PFC/JA-88-15

Plasma Production and Heating by ICRF in the Central Cell of the Tara Tandem Mirror

S. N. Golovato, K. Brau, J. Casey, J. Coleman, M. J. Gerver, W. Guss, G. Hallock[a], S. Horne, J. Irby, R. Kumazawa[b], J. Kesner, B. Lane, J. Machuzak, T. Moran, R. Myer, R. S. Post, E. Sevillano, D. K. Smith, J. D. Sullivan, R. Torti, L. Wang, Y. Yasaka[c], X. Z. Yao[d], J. Zielinski[a]

Plasma Fusion Center
Massachusetts Institute of Technology
Cambridge, MA 02139

April 1988

[a] Permanent address: Department of Electrical Engineering, University of Texas, Austin, TX.

[b] Permanent address: Institute of Plasma Physics, Nagoya University, Nagoya, Japan.

[c] Permanent address: Department of Electronics, Kyoto University, Kyoto, Japan.

[d] Permanent address: Institute of Physics, Beijing, China.

Submitted to: Physics of Fluids

This work was supported by the U. S. Department of Energy Contract No. DE-AC02-78ET51013. Reproduction, translation, publication, use and disposal, in whole or in part by or for the United States government is permitted.

ABSTRACT

Plasma production and heating by ICRF excitation using a slot antenna have been studied in the central cell of the Tara tandem mirror. Plasmas with a peak $\beta_\perp$ of 3%, density of $4 \times 10^{12}\ cm^{-3}$, ion temperature of 800 eV, and electron temperature of 75 – 100 eV were routinely produced. The plasma radius decreases with increasing ICRF power, causing reduced ICRF coupling and saturation of the plasma beta. Fifty to seventy percent of the applied ICRF power can be accounted for in direct heating of both ions and electrons. Wave field measurements have identified the applied ICRF to be the slow ion cyclotron wave. In operation without end plugging, the plasma parameters are limited by poor axial confinement and the requirements for maintenance of MHD stability and microstability.

I. INTRODUCTION

The application of radio frequency (RF) power in the ion cyclotron frequency range (ICRF) in the central cell of a tandem mirror has been shown to provide start up [1,2], ion heating[1-3] electron heating[4], and stabilization against magnetohydrodynamic (MHD) instability.[5] Advantage may be taken of all of these effects to improve tandem mirror performance. Starting up the plasma in the central cell and building to high temperature and density using fundamental resonance ion cyclotron resonance heating (ICRH) provides the necessary initial conditions in the plug end cells for thermal barrier and sloshing ion build up. Sloshing ions in combination with electron cyclotron heating (ECH) for creation of thermal barrier and plugging potentials has been proposed as a means of producing strong end plugging without the need for high density.[6] The required initial conditions in the plugs are low neutral pressure to minimize charge exchange losses, sufficient stream line density for sloshing ion build up, and sufficient stream ion temperature to minimize collisional filling of the thermal barrier.[1] The stabilization properties of ICRF can allow operation of a tandem mirror in purely axisymmetric geometry[7], eliminating the predicted resonant neoclassical radial loss of ions associated with quadrupole mirror fields.[8] ICRF stabilization of MHD modes in mirrors has been attributed to the ponderomotive force.[5,9]

This paper reports the properties of the ICRF heating that have been observed in the central cell of the Tara tandem mirror experiment. The stability properties of the plasma, including both MHD stability and microstability, are discussed in a separate paper.[10] The Tara central cell had a unique magnetic configuration which allowed the excitation of a slow wave for ion cyclotron heating at a beach resonances. The slow wave was identified by magnetic probe measurements in the plasma. The wave propagation and heating geometry of this experiment are very similar to those of ICRH experiments in the straight sections of the Model-C stellarator, where a slow wave antenna was used to heat at a beach resonance. [11] Other tandem mirrors have used fast wave heating with $\omega \gtrsim \omega_{ci}$, or non-resonant heating, with $\omega < \omega_{ci}$ everywhere in the central cell.[2,3] The slow wave heating produced hot mirror-trapped ions. Indications of direct electron heating by the ICRF were also seen. The plasma parameters were limited by the requirements to mainatin MHD stability and

microstability and by the absence of end plugging.

The paper is organized as follows. Section II will describe the unique central cell configuration of the Tara experiment. Section III discusses the ICRF startup of Tara, explaining the timing of the various systems, the plasma parameters achieved, and how they are measured. Section IV will discuss in more detail the properties and scaling of the plasma produced by the ICRF. The ion and electron power balances are presented in Sec. V. Measurements of the wave fields in the plasma and comparison with a theoretical model are presented in Sec. VI. Section V presents conclusions based on the results described in the previous sections.

II. CENTRAL CELL CONFIGURATION

The Tara experiment has several distinguishing features when compared to other tandem mirrors. The 10 m solenoidal central cell is bounded on each end by an axisymmetric plug cell followed by a transition to a minimum-$|B|$ anchor cell. A unique magnetic geometry and antenna design have been employed in the central cell to optimize central cell start up of a tandem mirror. This has been reported in a previous paper.[1] A local maximum (bump) in the magnetic field of mirror ratio 1.8 in the midplane region of the central cell is used as a source region for both ICRF excitation and gas fueling. The geometry is shown in Fig. 1 It allows excitation of ICRF in a region where the wave frequency, ω, is less than the local ion cyclotron frequency, ω_{ci}, so that the slow, ion cyclotron wave can be effectively coupled to the plasma for ion heating at "beach" resonances near the minimum magnetic field regions (wells) on either side of the bump. An aperture or slot antenna is used to excite the slow ion cyclotron wave. It is shown in Fig. 2, and has the following properties:

(1) low inductance, compared to the more commonly used loop antennas, coupling high power at lower voltage,

(2) strong coupling of the RF magnetic flux to the plasma, since there is little private flux around the antenna elements that does not link the plasma,

(3) antenna currents parallel to the magnetic field producing a parallel RF electric field, E_z, which provides efficient breakdown by coupling power to electrons in vacuum and in low density plasma,

(4) a wavelength spectrum which peaks at roughly twice the width of the antenna aperature, so that the shorter wavelength slow wave is preferentially excited over the fast wave.

Fueling on the bump isolates the cold gas from both the wells and the plug cells, minimizing charge exchange losses. Since there is an ion cyclotron resonance on each side of the bump, all cold ions from the gas box region must pass a resonance before exiting the central cell. They are efficiently trapped in the well mirrors and heated by the ICRH.[12] This configuration eliminates the problem of cold ions streaming into the plug cells.

An additional feature of the central call, as shown in Fig. 1 , is an axisymmetric magnetic divertor located on the midplane bump. This provides MHD stabilization in combination with the ICRF.[13] With these two stabilization mechanisms, it is not necessary during start up to provide stabilization by building up β (the ratio of the plasma energy density to the magnetic field energy density) in the outboard anchor cells. ICRH-produced ion β in the anchors [14] is necessary to provide stabilization during plugging experiments, which are otherwise driven unstable by sufficiently strong ICRH or ECH in the plug cells.

The data presented in this paper are from central cell plasmas created and maintained in steady-state by ICRF excited by the slot antenna. For these experiments no plasma was built up in the plugs by ICRH or ECH, or in the anchors by ICRH. Only the central cell end loss was flowing through these end cells. Thus there was no pressure weighting of either the good curvature of the anchors or the bad curvature of the plugs to affect MHD stability. The divertor was generally in operation for these experiments but it was not essential for maintaining MHD stability. The main effect of the divertor was to broaden the range of conditions where stable operation could be achieved.

III. ICRF CENTRAL CELL STARTUP

Plasma breakdown in the central cell is achieved by first providing a low density seed

plasma using ECH in an anchor cell. The seed plasma density is less than 10^{12} cm^{-3} in the anchor and less than 10^{11} cm^{-3} in the central cell. The presence of hot electron β in the anchors[14] has been shown to have no effect on the overall MHD stability of the Tara plasma, so this means of startup is benign in this respect. Anchor ECH is not necessary for breakdown but reduces the amount of gas that must be puffed into the central cell in advance of the ICRF pulse to achieve breakdown. This is desirable both to reduce charge exchange in the wells and to maintain control of the fueling in the gas box. The gas fueling is started 20-25 msec before the ICRF in order that breakdown occur at ICRF turn on. Hydrogen was used for all of the experiments described in this paper. The gas fueling rate ranged from 10-30 Torr-liters/sec with 20 Torr-liters/sec a typical value. Half of the fueling current is measured as end loss current, giving an overall gas fueling efficiency of 50%.[15] Figure 3 shows a typical time evolution of the basic signals used to characterize the plasma. Typically the ICRF is run for a 60 msec pulse at approximately constant power. The breakdown and build up to peak density takes about two milliseconds while the diamagnetism tends to rise more slowly, in about 4-5 milliseconds. Both the ICRF power and the gas fueling can be controlled during the shot to fine tune or vary conditions. Table I lists the diagnostics used to acquire the data in this paper and the parameters they measure.

The plasma parameters that have been achieved are summarized in Table II. This is a simultaneous data set with maximum values of the various parameters, which are seen under special conditions, shown in parentheses. The mirror-trapped ions in the two magnetic wells are the most energetic component of the plasma. These hot ions are produced by cyclotron damping at the fundamental ion cyclotron resonance ($\omega = \omega_{ci}$), which occurs along the magnetic field gradient or beach on either side of the bump.

One important feature of the plasma is an asymmetry between the plasmas in the two central cell magnetic wells. In general, the plasma in the south well has 2-3 times higher average ion energy than the north, although they have similar densities. The south well parameters are shown in Table II. The energy asymmetry is due to the shorter distance between the gas box and the north well, as shown in Fig. 1 . Although the slot antenna is on

the south side of the bump, RF magnetic probe measurements (which are discussed in Sec. V.) did not show an asymmetry in the ICRF field levels in the two wells. The higher neutral pressure which extends to lower mirror ratio in the north leads to greater charge exchange losses there. When the gas fueling is decreased during a shot, the density drops in the north and south wells, but the stored energy actually increases in the north while decreasing in the south, showing the sensitivity of the north to gas. The electron temperature is the same in the two wells, as confirmed by comparison of Thomson scattering data in the north well and double probe data in both the gas box and the south well. In the remainder of the paper south well parameters will be quoted unless otherwise mentioned.

IV. CHARACTERISTICS OF THE ICRF-HEATED PLASMA

There are three principal external variables that allow the control and study of the characteristics of the central cell plasma. These are the gas fueling rate, the ICRF power, and the resonance location.

Gas fueling variation

The variation of the gas fueling rate changes the radial profile of the plasma but only weakly affects the peak density, n_p. The radial density profile is measured by a four chord interferometer array. The data are best fit by a Gaussian profile with an e-folding radius, r_p, in the range of 1/2 to 2/3 of the limiter radius of 20 cm.[16] This differs from the profiles found in plasmas heated by fast waves at $\omega \gtrsim \omega_{ci}$, where broad flat profiles are seen.[7] Varying the gas fueling rate changes r_p much more strongly than n_p, as shown in Fig. 4 , where n_p, r_p, and the total number of particles, N_p, are plotted vs. gas fueling rate. N_p increases with fueling rate due primarily to the broadening of the radial profile. At the highest fueling rates, n_p decreases, with the profile flattening in the center and building up at the edges. The saturation of n_p appears to be due to shielding of the gas from the core as the edge density builds up.[15]

ICRF power variation

When the ICRF power is increased, the stored energy in the plasma increases and then

saturates. This is illustrated in Fig. 5 , where the stored energy in the plasma, W_p, central line density, nl_0, line density at $r = 14cm$, nl_{edge}, and antenna load resistance, R_{load}, are plotted vs. ICRF power for two conditions. The plus signs, corresponding to a gas fueling rate of 20 Torr-liters/sec, show the saturation of W_p with increasing ICRF power. The diamonds, corresponding to 28 Torr-liters/sec, show no saturation. The saturation may be explained by effects on the radial density profile, as shown by the variation of nl_0 and nl_{edge}. The raw line densities are used because they show the effect more clearly than the peak density and radius derived from a fit to line density data. For the lower fueling rate case, nl_{edge} decreases strongly with increasing power and nl_0 saturates. The reduction in nl_{edge} with power has the effect of increasing the distance between the antenna and the plasma. This reduces the coupling to the plasma, causing R_{load} to decrease, as Fig. 5 shows. The saturation of W_p as R_{load} decreases implies that the power to the core plasma remains roughly constant even though the total applied power is increasing. The core plasma refers to the central region of the plasma where energy confinement is better due to shielding of neutral gas. The drop in R_{load} of only 15%, if entirely due to reduced core coupling, represents a large reduction in the percentage of the applied power going to the core. Note that the zero has been suppressed in the R_{load} graph to show the drop more clearly. From the ion power balance, which is discussed in the next section, only about 25% of the applied power goes to the hot ions, which make the largest contribution to W_p. The saturation of the heating can be circumvented by increasing the fueling rate, which broadens the plasma (as shown in Fig. 4). The higher fueling rate data in Fig. 5 show that nl_{edge} and R_{load} decrease more slowly with power, and the saturation of W_p would be expected to occur at a higher power level than was available when this data set was taken. Power levels up to 600 kW were subsequently applied and the saturation effect was observed at higher gas fueling rates.

The saturation of W_p at high power does not appear to be related to instability. As is discussed in the companion stability paper[10] , MHD stability is enhanced at higher power. The lower values of W_p and nl_0 seen in Fig. 5 for the low gas fueling case at low ICRF power are due to low levels of MHD instability.[10] Microinstability has been observed to

limit energy confinement when the plasma is highly anisotropic.[10] However, neither the anisotropy of the plasma nor the level of the observed micro-unstable mode increases with increasing ICRF power.

The decrease in nl_{edge} with power does not necessarily imply that radial transport is generated by the ICRF. It may be that this is a property of the equilibrium, where the radial profiles of the fueling, heating, and ICRF stabilization [10] must be appropriate to produce a stable plasma configuration.

Resonance location variation

The location of the ion cyclotron resonance along the gradient between the bump and the wells was varied by changing the magnetic field only in the well regions and keeping the frequency of the ICRF constant. In this way the ICRF excitation on the bump is not changed. Figure 6 shows the variation of $\beta_\perp$, and peak density, n_p, with ω/ω_{ci} at the magnetic well minimum field, ω/ω_{ci0}. The abscissa values are also the mirror ratio where the resonance occurs. For abscissa values less than one, there is no resonance in the central cell. Eliminating the resonance still allows ions with sufficient parallel velocity to be heated since the resonance occurs at $\omega - k_\| v_\| = \omega_{ci}$ ($k_\|$ and $v_\|$ are respectively the wave number and velocity parallel to the magnetic field). The data in Fig. 6 show that the highest $\beta_\perp$ and n_p are produced with the resonance close to the minimum field of the well ($\omega/\omega_{ci} = 1.05 - 1.15$) but not at minimum itself.

Varying the resonance location affects the heating efficiency by changing the magnetic field gradient at the resonance. This changes the distance over which the resonant interaction between the ICRF and the ions occurs as the ions move through the resonance region during their bounce motion in the well mirrors. The strongest resonant interaction should occur in the long minimum field regions of the well producing the best heating.[12] However, $\beta_\perp$ is largest with the resonance up on the gradient. This may be understood by looking at the anisotropy of the hot ions as a function of resonance location.

The anisotropy of the hot, mirrored-trapped ions is represented by $p_\perp/p_\|$ ($p_\perp$ and $p_\|$ being the ion perpendicular and parallel pressures). The anisotropy of the hot ions is

calculated using the ratio of signals from two diamagnetic loops, one at the magnetic well midplane and one at a mirror ratio of approximately 1.1 along the gradient toward the bump.[17] Figure 7 shows that the hot ion pressure anisotropy increases as the resonance is moved closer to the well midplane. This occurs because ICRH increases the ion perpendicular velocity at the resonance location. When the resonance is not at the midplane this corresponds to a change in both the perpendicular and parallel velocity of the ion at the midplane. The ratio of perpendicular to parallel velocity, and therefore the anisotropy of heated ions, increases as the resonance is moved toward the midplane, as seen in Fig. 7 . Data from the gridded end loss analyzers and end loss ion spectrometer show that the temperature of the ion end loss increases as the resonance is moved away from the well midplane, indicating that the ICRH is producing more parallel heating.

A consequence of the high $\beta_\perp$ and anisotropy when the resonance is very close to the well midplane is the observation of an ion microinstability. The instability has been identified as the Alfvén ion cyclotron mode, and is discussed in detail in Ref. 10. The instability appears to limit $\beta_\perp$ under conditions where the heating is strongest.

V. ION AND ELECTRON POWER BALANCE

The goal of the analysis presented here is to account for the applied ICRF power in the plasma rather than to analyze the confinement properties of the device. A detailed analysis of the particle and power loss mechanisms from the plasma in Tara is presented elsewhere. [15,18]

Ion power balance

The ICRF power input to the hot mirror-trapped ions in the central cell wells may be estimated by looking at the decay rate of the diamagnetism when the ICRF power is abruptly decreased. The diamagnetic loop decay was obtained by modulating the power by about 25%. Turning off the power completely caused immediate MHD instability and a much faster decay. Dividing the stored energy (from Fig. 5) by the decay time gives the power to the hot ions. For 300 kW of applied power, the stored energy was 75 Joules and the decay time 1 msec, yielding a heating power of 75 kW.

The total ion power balance for the central cell may may be described by

$$P_{RF} = I_{loss} T_{i_{loss}} + \frac{n(T_{i_w} - T_e)V_w}{\tau_d} + n n_{0_w} T_i V_w \langle \sigma v \rangle_{cx_w} + n_{gb} n_{0_{gb}} T_{i_{gb}} V_{gb} \langle \sigma v \rangle_{cx_{gb}}. \quad (1)$$

Here n is the plasma density, n_0 the atomic hydrogen density, T_i the ion temperature, V the plasma volume, $\langle \sigma v \rangle_{cx}$ the charge exchange rate coefficient, I_{loss} the ion end loss current, $T_{i_{loss}}$ the ion end loss temperature, T_e the electron temperature, and τ_d the electron drag time (assuming $T_i > T_e$).[19] Subcript w refers to the wells and gb to the gas box. The left hand side of Eq. (1) represents the power input to the ions from the ICRH. The right hand side contains the power losses from end loss, collisional equilibration with the colder electrons and charge exchange.

Using the conditions described in Table II, these terms may be estimated. For $T_{i_{loss}} = 200\ eV$ and the end loss ion current of 150 amps, the ion end loss power was 30 kW. The drag power was 15 kW. Losses due to neutral gas require the knowledge of the radial profile of the neutrals. The atomic and molecular hydrogen densities and profiles have been estimated using a laser fluorescence diagnostic, H_α measurements, and modelling with codes.[20] From this analysis the charge exchange power in the well is calculated to be 5 kW. The gas box charge exchange loss is difficult to estimate since the temperature and density of the passing ions (those mirror-trapped in the central cell but not in one of the wells) were not directly measured. It can be inferred using the known ionization source, the end loss ion temperature of 200 eV, and the ratio of the charge exchange to ionization rates, which is about two for $T_e = 100\ eV$ and $T_i = 200\ eV$. For the ionization source of about 300 atom-amps, the gas box charge exchange loss would be 120 kW. Another estimate can be made by using the measured neutral pressure in the gas box, the end loss ion temperature, and a density on the bump of 2/3 the well density (a measurement made before the divertor was installed). The neutral pressure in the gas box is two orders of magnitude higher than in the wells. This gives a power loss from charge exchange in the gas box of about 90 kW, in reasonable agreement with the first estimate. Summarizing, the ion losses account for about 140-170 kW of the applied ICRF power of 300 kW, 75 kW from the hot ions in the wells and the rest from the passing ions.

Electron heating

The electron temperature was measured by radially scannable Thomson scattering in the north well and by a double probe in the outer third of the plasma. Typically T_e was $60 - 80\ eV$ on axis increasing to $100 - 120\ eV$ at $r = r_p$.[13] T_e decreases with increasing gas fueling and increases with increasing ICRF power in the core and at the edge. The variation of T_e with resonance position is shown in Fig. 8 . T_e is highest for $\omega/\omega_{ci0} < 1$, where there is no ion resonance and there is little ion heating, as was seen in Fig. 6 . This is strong evidence that there is direct electron heating by the RF, since T_e is high even when the ion temperature is low and there was little power flow to the electrons from hotter ions. Direct electron heating has been seen in other experiments and has been attributed to Landau damping.[21] Using $T_e = 80\ eV$, the electron thermal velocity would equal the wave phase velocity for $k_{\|}$=0.04 cm^{-1}, which is reasonable for the slow wave, as will be shown in Sec. VI. Codes which model the RF fields in this frequency range typically predict a small E_z on axis which increases with radius.[22] These conditions are consistent with electron heating by Landau damping and the hollow T_e profile that is observed.

Other evidence that supports direct electron heating comes from the electron power balance, which may be written

$$P_{RF} + \frac{n(T_i - T_e)V_w}{\tau_d} = I_{loss}(T_e + \phi_e) + nn_0 E_{ion} V_{gb} \langle \sigma v \rangle_{ion} \ . \qquad (2)$$

Here ϕ_e is the central cell plasma potential, E_{ion} the energy loss per ionization, and $\langle \sigma v \rangle_{ion}$ the ionization rate. Describing the terms in Eq. (2) from left to right, the power inputs to the electrons on the left hand side are from direct RF heating and electron drag on the hotter ions. The losses on the right hand side are primarily from end loss and collisions with neutral hydrogen gas. The end loss power includes both the energy of the lost electron and the power necessary to overcome the positive potential between the central cell plasma and the grounded end wall. The electron-neutral collisional losses include the ionization power as well as associated excitation radiation from both atomic and molecular hydrogen. This occurs primarily in the gas box and is concentrated toward the edge where the neutral density is highest. Estimates of the terms in Eq. (2) may be made for the conditions described in Table II. The electron end loss current is assumed to equal the ion end loss current. A net electron current at the end wall, which is indicative of non-ambipolar radial

loss of ions, was measured to be less than 10% of the total end loss current for these experiments. The electron end loss power is 60 kW. The losses associated with neutral gas are calculated to be 10-20 kW. The drag power is only about 15 kW, requiring direct RF heating power of 55-65 kW.

The total power to electrons can be estimated in another way. When ECH is applied to one of the plug cells, T_e is increased in the central cell. This is seen by Thomson scattering and by the HIBP, which measures the associated potential increase. The HIBP has a fast time response and follows the potential, and therefore T_e, decay when the ECH is turned off. The decay time, τ_e, is about 200 μsec. Since the density is not changed by the ECH, this represents a measure of the electron energy confinement time. The total power to the electrons may be estimated as

$$P_e = \frac{n_p T_e V_{cc}}{\tau_e} \ , \tag{3}$$

where the plasma volume, V_{cc}, in this case would be the entire central cell. Using the τ_e measured in the plug ECH turnoff experiment, P_e is calculated to be 80 kW during central cell ICRF heating. This is consistent with the power balance estimate and supports the hypothesis of direct electron heating.

The electron losses of 70-80 kW and the total ion losses of 140-170 kW (with drag not included since it is a transfer rather than a loss) make up about 65-78% of the 300 kW of ICRF power. The unaccounted power may be carried out by the 50% of the gas fueling that does not show up as end loss. All of the gas should be ionized in the gas box, and half of these cold ions are apparently lost radially in the gas box region.[15] Some power may also be deposited at the edge and flow to limiters, but this has not been measured.

VI. WAVE FIELD MEASUREMENTS

In order to better understand the physics of the observed ICRF heating and stabilization, the wave fields were measured in the plasma by RF magnetic field probes. The goals were to identify wave modes excited in the plasma through measurement of the axial wave number and to measure the wave number and magnetic field radial profiles.

The RF probes were designed to measure only magnetic fields, to have adequate frequency response, and to have sufficient signal level to be used without amplifiers. Each probe consisted of three orthogonal coils to measure the three magnetic field components simultaneously. Each coil had six 3 mm diameter turns with a grounded centertap. They were electrostatically shielded and were covered by a 7 mm Pyrex or quartz tube. The coils were connected through a 1:1 RF transformer to 50 Ω inputs of 32 MHz digitizers and could measure 1 Gauss fields at 3.5 MHz.

The data from as many as eight coils per shot were analyzed using fast Fourier transform techniques.[23] Both the amplitude and relative phase were calculated not only for the excited ICRF at 3.47 MHz but also a plasma-generated mode, which will be described in the next section. The probes were calibrated on a test stand and instrumental phase shifts were taken into account. The perturbation of the plasma by the probes was small except when they were inserted close to the magnetic axis ($r < 6cm$). Three probes were spaced 30 cm apart axially along the gradient between the bump and the north well midplane to measure the axial wave number as well as the field amplitudes. Probes were also distributed azimuthally at one axial position to measure the azimuthal structure of the mode.

The wave mode excited in the plasma was identified by measuring the axial wave number, k_z, from the phase shift between the three probes spaced axially along the gradient. The scaling of k_z with ω/ω_{ci} is shown in Fig. 9 The data consist of two measured values of ω/ω_{ci} per shot for a scan of the magnetic well field, which varies ω/ω_{ci} on a shot to shot basis. The probes were at r=13.5 cm. The solid lines in the figure are the parallel wave number predicted by cold, homogeneous plasma theory for the slow ion cyclotron wave,

$$k_{\|} = \frac{\omega}{\omega_{ci}} \frac{\omega_{pi}}{c} \frac{1}{(1-(\omega/\omega_{ci})^2)^{1/2}} \cdot \tag{4}$$

Here ω_{pi} is the ion plasma frequency, making $k_{\|}$ scale as $n^{1/2}$, and $k_{\|} = k_z$ for this experiment. The upper line is for a density of $1 \times 10^{12} cm^{-3}$ and the lower for half this density. These are reasonable values for the radius where the measurements were made. The lower density is appropriate for the data at lower values of ω/ω_{ci} where the plasma

is typically less dense (see Fig. 6). The data show reasonable agreement with the cold plasma model over a wide range of conditions, indicating that the excited mode is indeed the slow wave. Figure 10 shows the scaling of k_z with radius. The k_z indicative of the slow wave was observed throughout the plasma. The lower value at 3 cm is due to the perturbation of the plasma by the probes. Except at the extreme edge beyond the limiter radius of 18 cm, there is no evidence of a significantly smaller k_z associated with the fast wave. The m=1 fast wave should propagate in this plasma[24] but it was apparently not excited in this combination of antenna and magnetic geometry. The density scaling of k_z in Eq. (4) did cause a small decrease in k_z with radius inside the limiter. The scaling of k_z with density was also studied by varying the gas fueling rate and agreed with the cold plasma model.

The radial structure of the RF magnetic fields for three axial locations along the magnetic field gradient is shown in Fig. 11 . Looking at the top plot, the profile of the azimuthal component, B_θ, peaks at r=10-12 cm. The profile of the radial component, B_r, has a broad peak at the plasma center, with a magnitude less than half the peak value of B_θ. B_z is not shown but has a lower magnitude than the other components. Similar profiles of B_θ were observed on probes at two other axial positions, as seen in the two lower plots in Fig. 11 . The data show that the form of the radial profiles does not vary substantially along the gradient between the point of excitation and the resonance.

The experimental results have been compared with a model for the wave propagation. This model, referred to as the McVey code[22] , has important features of the experiment such as the radial profiles of plasma parameters and the geometry of the slot antenna. Finite temperature effects are included to allow for electron Landau damping and the effect of the Doppler shift on the ion cyclotron damping. Its applicability to this experiment is limited since it does not include the effect of the axial gradient in the magnetic field. However, to the extent that the code results are consistent with the RF magnetic field measurements, the code may be used to estimate the difficult-to-measure RF electric fields. A knowledge of electric fields is necessary to understand such details of the observed heating and stabilization as the radial distribution of the heating and the ponderomotive force.

Because the McVey code model assumes an axially uniform magnetic field, it is necessary to choose a single value for ω/ω_{ci}. The coupling to the slow wave will be incorrect if the magnetic field is chosen too close to resonant, since the wavelength is too small near the resonance to be effectively excited by a realistic antenna. Using the value of the magnetic field under the antenna agrees best with the experiment since the excitation region is modelled correctly. However, the ion absorption will not be correct since the code will predict little cyclotron damping for $\omega/\omega_{ci} = 0.65$, the value at the antenna in the experiment. Figure 10 included McVey code results (represented by X's) for the variation of k_z with radius. The lower values of k_z predicted by the code are due in part to the lower ω/ω_{ci} used in the code compared to that at the measurement location ($\omega/\omega_{ci} = 0.81$). Using Eq. (4) to scale the code data to the same ω/ω_{ci} as the experimental data gives a factor of 1.6. The code results then agree well with the measurements for r$\leq$10 cm and beyond the limiter radius of 18 cm, but do not agree at r=15 cm. The code predicts a smaller k_z indicative of the fast wave which was not observed in the experiment.

A comparison of the McVey code radial profile with the experiment is shown in Fig. 12 for two azimuthal angles. The form of the radial profile is similar for r<15 cm and the magnitude of the code results have been multiplied by 2/3 to better match the experiment. This is quite good agreement considering the uncertainties in the probe calibrations and the value of RF magnetic field in the antenna aperature, which is the required input for the code to model a slot antenna. The most obvious difference between the code and the experiment is the absence in the experiment of the large edge fields predicted by the code. The $m = 1$ fast wave which produces the high edge fields in the code was apparently not strongly excited in the experiment, as was also indicated by the k_z measurements. This is most likely due to the magnetic configuration, since the code should model the antenna spectrum accurately. The second maximum in the radial profiles occurs at r=10-12 cm in both the code and experiment. The exact radius of the maximum is dependent on ω/ω_{ci}, the radial density profile, and the axial distance from the antenna. Figure 12 uses the measured values of these quantities and shows reasonable agreement. The details near $r = 0$ apparent in the code results are difficult to measure in the experiment due to the

large perturbation of the plasma when the probes are near the center.

Since the wave physics in the resonance region has not been modelled correctly, the code results are not useful in calculating ion cyclotron damping rates and absorption profiles. Calculations using the code results in the ponderomotive model for ICRF stabilization of MHD instability may have more relevance since the code appears to model reasonably the radial profiles of the wave fields. This is discussed in Ref. 10.

V. CONCLUSIONS

Slow wave excitation and propagation into beach resonances have been shown to effectively produce high β central cell plasmas. The slow wave character of the applied ICRF was measured with magnetic probes and agrees reasonably well with both the cold plasma model and the McVey code. The central cell parameters produced in these experiments represent an optimization of the plasma achievable in this unplugged, axisymmetric mirror configuration in the following sense.

Charge exchange has been minimized by use of a localized, small volume gas source on a magnetic bump. The height of the bump cannot be increased to better isolate the mirror-trapped hot ions in the wells from the gas because this leads to MHD instability.[10] The electron energy confinement appears classical, with the electron temperature limited by end loss and losses associated with ionization of the cold fueling gas.

Lower gas fueling rates reduce both electron and ion energy losses. However the plasma radius is reduced under conditions of low gas fueling and high ICRF power, causing a decrease in ICRF coupling and saturation of the stored energy. Low gas fueling also leads to lower MHD instability thresholds.[10] The gas fueling must be kept sufficiently high to maintain the ICRF coupling and MHD stability.

Unfortunately higher fueling rates do not increase the peak density, since the cold gas fueling from the edge does not penetrate sufficiently to the plasma center.[15] The slow wave coupling to the core also has a density limit for a given antenna spectrum.[11] The limits to core fueling and heating illustrate the importance of improved particle confinement (end

plugging) for increasing the central cell density of the tandem mirror. If axial confinement is sufficiently improved, higher densities can be maintained at lower gas fueling rates, improving energy confinement. MHD stability may still be a problem if the gas fueling is too low.[10]

The heating cannot be improved by moving the resonance location. The resonance location for best heating is bracketed by MHD instability when it is too far off the midplane and microinstability when it is too close to the midplane.[10] Improved axial confinement and lower gas fueling would improve the heating since hot ions would have to undergo more pitch angle scattering to be lost, reducing the anisotropy which drives the microinstability. The longer axial extent of a plugged central cell plasma would, however, increase the MHD drive.

Although there may be some subtle tuning of conditions that will result in incremental improvement in the central cell parameters, the reduction of end losses is the clear direction to bring about dramatic improvement. This is of course the goal of tandem mirrors. MHD stability is still a major concern in axisymmetric geometry but additional magnetic divertors might alleviate this. The results reported here show the strengths of slow wave excitation for plasma production and heating and the limitations imposed by simple mirror confinement.

ACKNOWLEDGEMENTS

It is a pleasure to acknowledge the support of the Tara tandem mirror engineering and technical staff whose work contributed greatly to the attainment of these results. In particular, the work of H. L. Holcomb on the RF systems and W. Brooks on the RF magnetic probes was greatly appreciated.

This work was supported by U. S. Department of Energy Contract No. DOE-AC02-78ET51013.

References

[1]R. S. Post, K. Brau, S. Golovato, E. Sevillano, D. K. Smith, W. Guss, J. Irby, R. Myer, and J. Sullivan, *Nuclear Fusion* **27**, 217 (1987).

[2]R. Goulding, PhD. Thesis, University of Wisconsin, 1987.

[3]G. Dimonte, A. W. Molvik, J. Barter, W. F. Cummins, S. Falabella, P. Poulsen, and T. Romesser, *Nuclear Fusion* **27**, 1959 (1988).

[4]S. Yoshikawa and H. Yamato, *Phys. Fluids* **9**, 1814 (1966)

[5]J. R. Ferron, N. Hershkowitz, R. A. Breun, S. N. Golovato, and R. Goulding, *Phys. Rev. Lett.* **51**, 1955 (1983).

[6]D. E. Baldwin and B. G. Logan, *Phys. Rev. Lett.* **43**, 1318 (1979).

[7]J.R. Ferron, R. Goulding, B.A. Nelson, T. Intrator, E.Y. Wang, G. Severn, N. Hershkowitz, D. Brouchous, J. Pew, R.A. Breun, and R. Majeski, *Phys. Fluids* **30**, 2855 (1987).

[8]J. Kesner, R.S. Post, B.D. McVey, and D.K. Smith, *Nucl. Fusion* **22**, 549 (1982).

[9]J.R. Myra and D.A. D'Ippolito, *Phys. Rev. Lett.* **53**,914 (1984).

[10]S. N. Golovato, K. Brau, J. Casey, M. J. Gerver, S. Horne, J. Irby, J. Kesner, B. Lane, J. Machuzak, R. Myer, R. S. Post, E. Sevillano, L.Wang, *Phys. Fluids* (submitted for publication).

[11]J. C. Hosea and R. M. Sinclair, *Phys. Fluids* **13**, 701 (1970).

[12]S. N. Golovato, R. A. Breun, J. R. Ferron, R. H. Goulding, N. Hershkowitz, S. F. Horne, and L. Yujiri, *Phys. Fluids* **28**, 734 (1985).

[13]J. A. Casey, B. G. Logan, J. H. Irby, K. L. Brau, S. N. Golovato, W. C. Guss, J. Kesner, R. S. Post, E. Sevillano, and J. Zielinski, MIT Report PFC/JA-87-25 (submitted to *Phys. Fluids*).

[14]K. Brau, B. Lane, J. Casey, S. Horne, J. Kesner, S. N. Golovato, J. H. Irby, R. S. Post, E. Sevillano, and D. K. Smith, *Nuclear Fusion* (to be published).

[15]E. Sevillano, K. Brau, J.A. Casey, S.N. Golovato, W.C. Guss, S.F. Horne, J.H. Irby, J. Kesner, B.G. Lane, T. Moran, R.S. Post, and J.D. Sullivan, *Phys.Fluids* (submitted for publication).

[16]J.H. Irby, B.G. Lane, J.A. Casey, K. Brau, S.N. Golovato, W.C. Guss, S.F. Horne, J. Kesner, R.S. Post, E. Sevillano, J.D. Sullivan, and D.K. Smith, *Phys. Fluids* (to be published).

[17]J. Kesner, private communication.

[18]E. Sevillano, K. Brau, J.A. Casey, S.N. Golovato, W.C. Guss, S.F. Horne, J.H. Irby, J. Kesner, B.G. Lane, T. Moran, R.S. Post, J.D. Sullivan, and J. Zielinski, *Phys.Fluids* (submitted for publication).

[19]D. E. Baldwin, *Rev. Mod. Phys.* **49**, 317 (1977).

[20]W. C. Guss, X. Z. Yao, L. Pócs, R. Mahon, J. Casey, S. Horne, B. Lane, R. S. Post, R. P. Torti, *Phys. Fluids* (submitted for publication).

[21]S. N. Golovato, B. D. McVey, J. E. Scharer, R. A. Breun, D. K. Smith, J. Yugo, and L. Yujiri, *Nuclear Fusion* **22**, 741 (1982).

[22]See National Technical Information Service Document No. DE85004960 ("ICRF Antenna Coupling Theory for Cylindrically Stratified Plasma," Massachusetts Institute of Technology Report PFC/RR-84-12 by B. McVey). Copies may be ordered from the National Technical Information Service, Springfield, Virginia 22161. The price is $16.95 plus a $3.00 handling fee. All orders must be prepaid.

[23]D. E. Smith, E. J. Powers, and G. S. Caldwell, *IEEE Trans. Plasma Sci.* **PS-2**, 263 (1974).

[24]F. J. Paoloni, *Phys. Fluids* **18**, 649, (1975).

Figure Captions

Figure 1. The Tara magnetic flux geometry showing the bump region, one of the central cell wells, and one axisymmetric end cell.

Figure 2. The slot antenna geometry with balanced feed.

Figure 3. The time evolution of the basic central cell diagnostics for a shot with parameters similar to those in Table II

Figure 4. The variation of the peak density, Gaussian radius, and total particles (per unit length axially) when the gas fueling rate was varied.

Figure 5. The variation of the total stored energy, the line density along central (r=0 cm) and edge (r=14 cm) chords, and the plasma loading of the slot antenna when the ICRF power was varied. The data represented by crosses are for a gas fueling rate of 20 Torr-liters/sec and by diamonds, a rate of 28 Torr-liters/sec.

Figure 6. The variation of the peak beta and peak density when the ion cyclotron resonance location was varied by changing only the magnetic well minimun field. The ratio of the RF frequency to the ion cyclotron frequency at the magnetic well minimum field is plotted on the horizontal axis. This is equivalent to the mirror ratio at the resonance location.

Figure 7. The variation of the anisotropy of the hot, mirror-trapped ions in the wells when the ion cyclotron resonance location was varied. Each point is the average of 2-3 shots and was computed using the ratio of signals from diamagnetic loops at mirror ratios of 1 and 1.1.

Figure 8. The variation of the electron temperature when the ion cyclotron resonance location was varied.

Figure 9. The measured axial wave number vs. the ratio of the RF frequency to the ion cyclotron frequency at the location of the measurement. These data (shown by diamonds) were obtained from measurements at two axial locations per shot by varying the magnetic

field from shot to shot. The solid lines are the cold plasma model for a densities of $1 \times 10^{12} cm^{-3}$ (upper line) and $5 \times 10^{11} cm^{-3}$ (lower line)

Figure 10. The axial wave number vs. radius. The data represented by diamonds are measured values and the X's are results of McVey code calculations.

Figure 11. The measured radial profiles of the RF magnetic fields in the plasma. The three plots are simultaneously obtained results for different axial locations along the magnetic field gradient. They correspond to ω/ω_{ci} values of (from top to bottom) 0.65, .075, and 0.87. The B_θ component is shown by diamonds and the B_r component in the top plot by squares.

Figure 12. A comparison of the radial profiles of B_θ obtained from experimental measurements (diamonds) and McVey code calcualtions (solid lines). The two plots are for different azimuthal angles at an axial location 195 cm from the antenna ($\omega/\omega_{ci} = 0.87$).

TABLE I

PARAMETER	DIAGNOSTIC
Density Profile (radial and axial)	Microwave Interferometer Arrays
Stored Energy and Anisotropy	Diamagnetic Loops
Ion Temperature (perpendicular)	Diamagnetic Loop
	Charge Exchange Analyzer
Ion Temperature (parallel)	Gridded End Loss Analyzer
	E||B End Loss Ion Spectrometer
Electron Temperature Profile	Radially Moveable Thomsom Scattering
	Impurity Line Ratios
	Double Probe
End Loss Ion Current	Faraday Cup Arrays
End Loss Net Current	Unbiased Detector Arrays
ICRF Power	Directional Coupler
Plasma Light Emission Profile	Light Detector Arrays With Filters
Ionization Source	End Wall TV Camera With H_α Filter
	Calibrated Gas Injection
Neutral Density Radial Profile	Laser Fluorescence
Neutral Density Axial Profile	Fast Ion Gauges
Charge Exchange Radial Profile	Scannable Secondary Emission Detector
Fluctuations	Electrostatic Probes
	Magnetic Probes
	Light Detectors
	140 GHz Gyrotron Scattering

TABLE II

PLASMA PARAMETER	SELF-CONSISTENT VALUE	BEST VALUE
Peak Density ($10^{12} cm^{-3}$)	4	6.5
Average Ion Energy (keV)	0.8	1.5
End Loss Ion Temperature (eV)	200	
Electron Temperature (eV)	75	120
Peak Beta (%)	2.6	3
Average Beta (%)	1	
ICRF Power (kW)	300	700
Global Energy Confinement Time (ms)	.15	.3
Ion Energy Confinement Time (ms)	1	
Parallel Confinement Time (ms)	2.5	
Non-ambipolar Radial Loss Time (ms)	20-100	

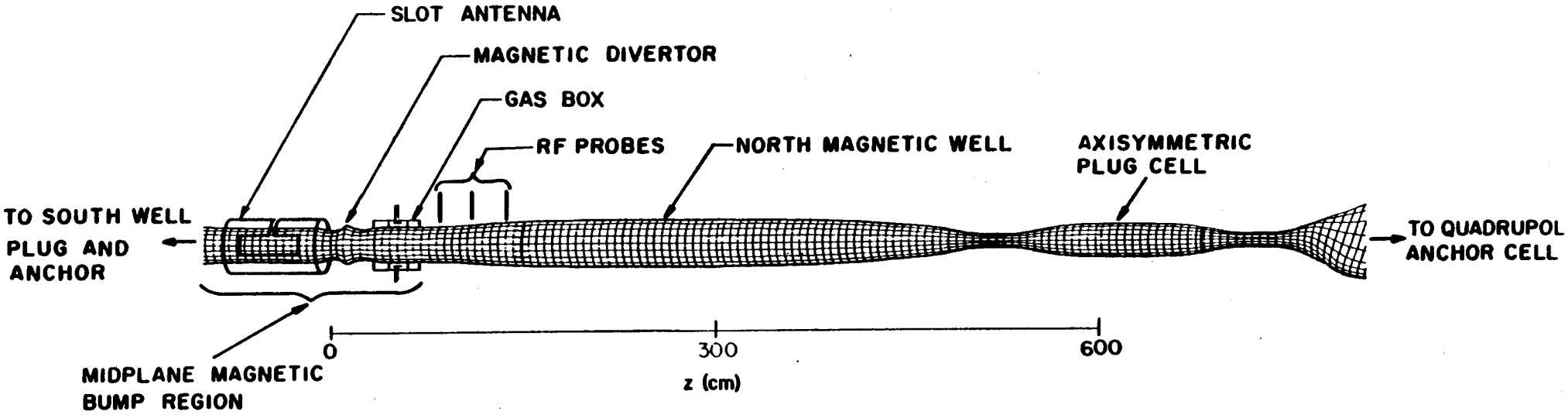

TARA MAGNETIC FLUX TUBE

Figure 1

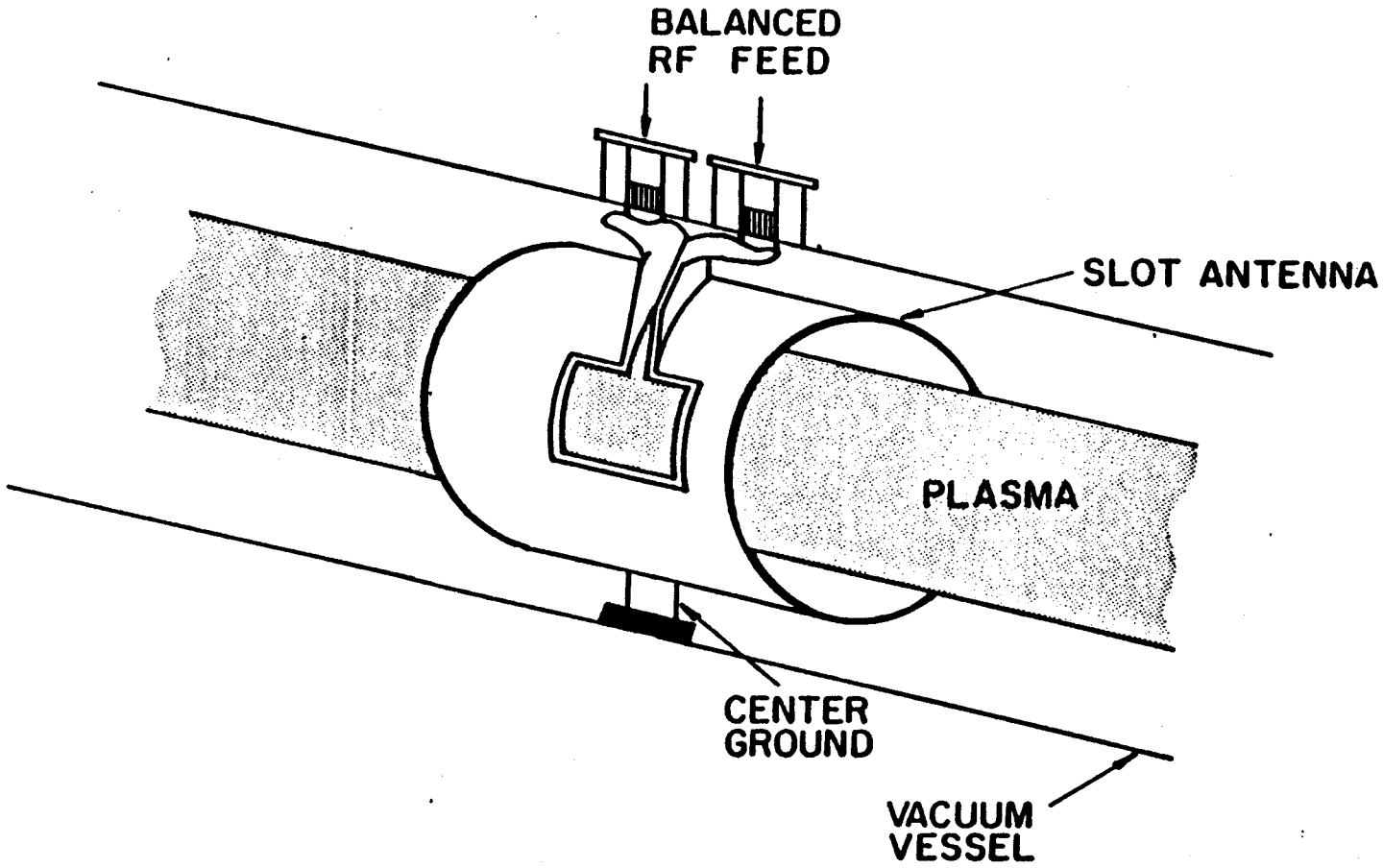
BALANCED
RF FEED
SLOT ANTENNA
PLASMA
CENTER
GROUND
VACUUM
VESSEL

Figure 2

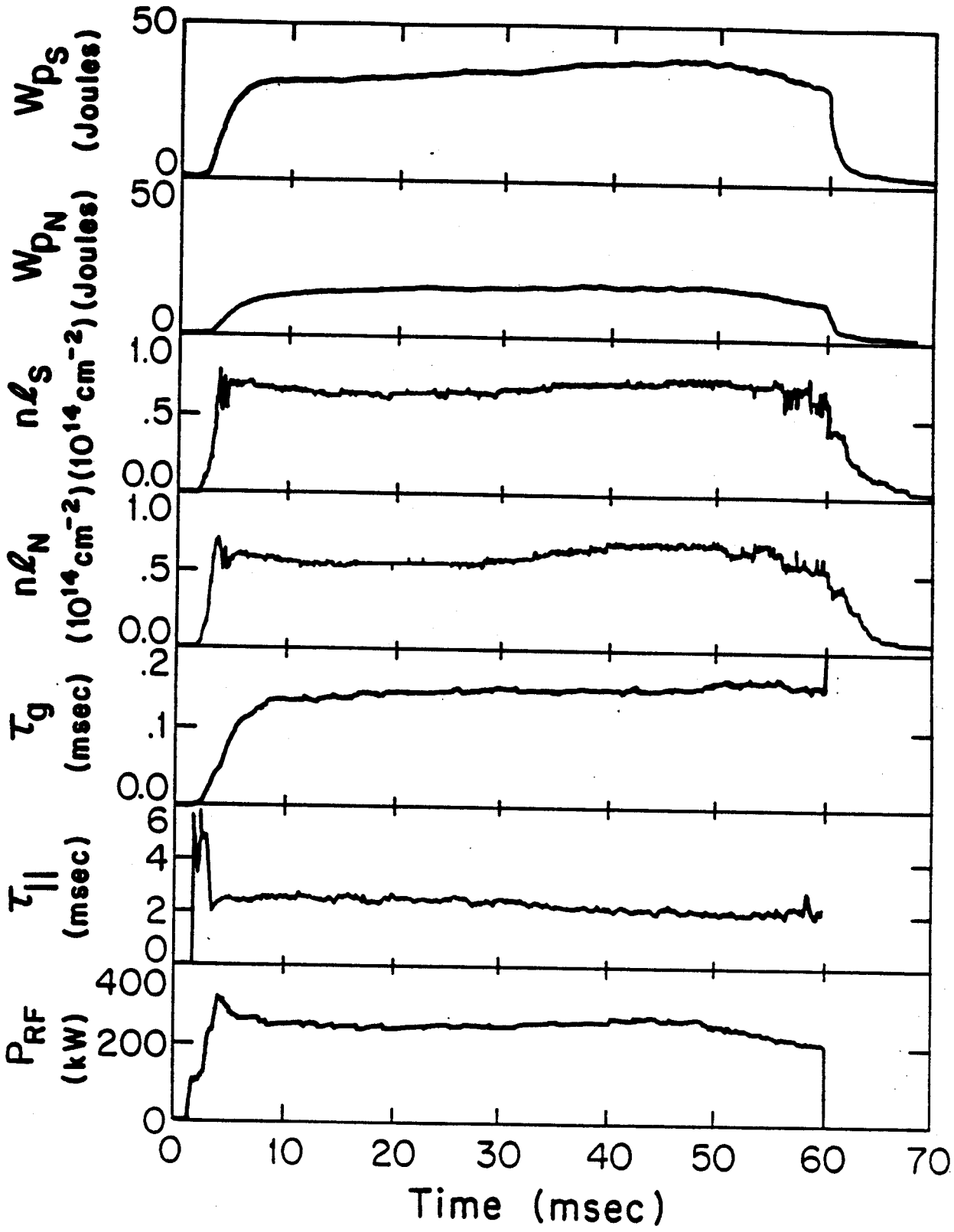
W_{p_S} (Joules)
50
0
W_{p_N} (Joules)
50
0
$n\ell_S$ $(10^{14}cm^{-2})$
1.0
.5
0.0
$n\ell_N$ $(10^{14}cm^{-2})$
1.0
.5
0.0
τ_g (msec)
.2
.1
0.0
$\tau_{||}$ (msec)
6
4
2
0
P_{RF} (kW)
400
200
0
0
10
20
30
40
50
60
70
Time (msec)

Figure 3

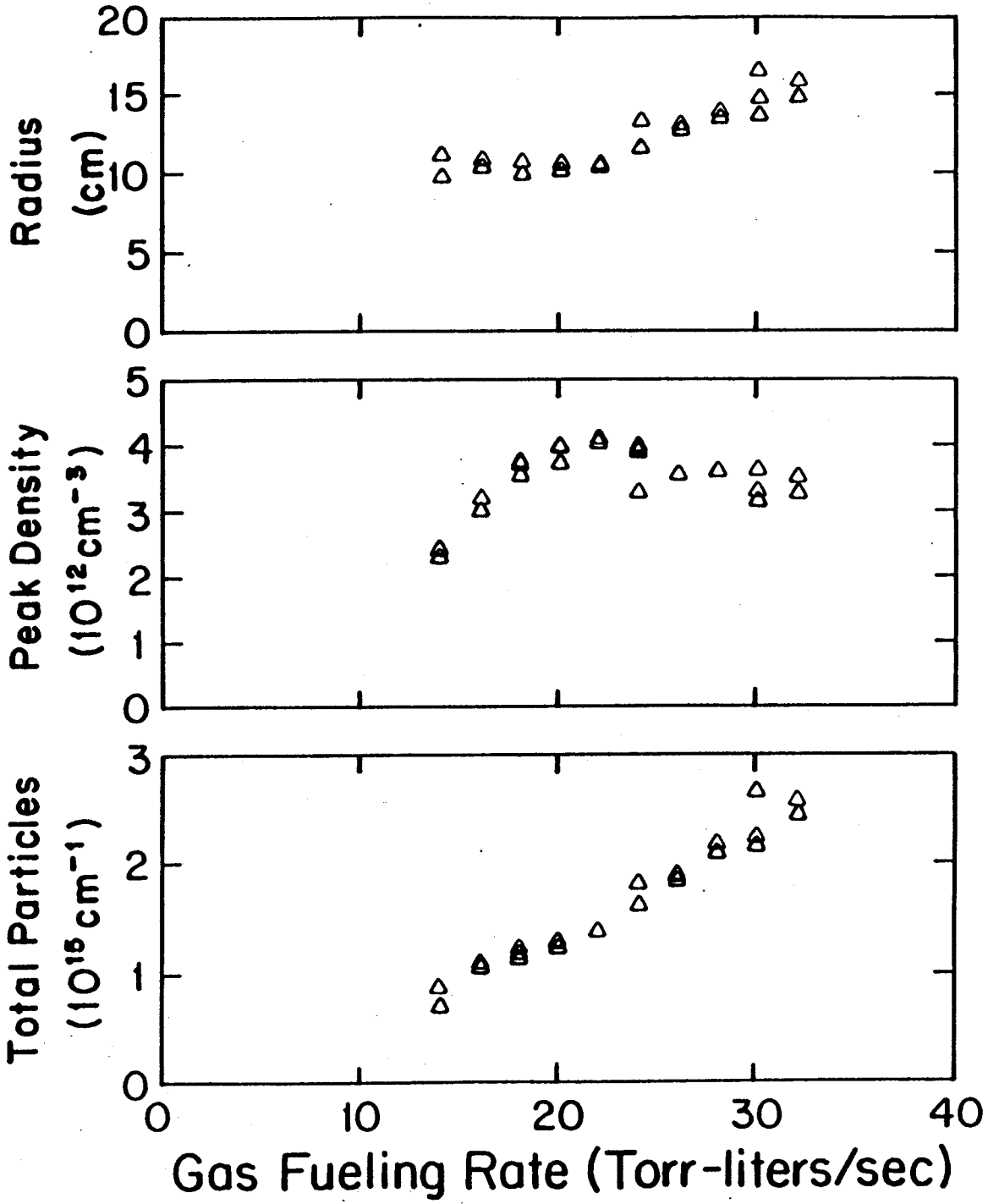
Radius (cm)
20
15
10
5
0
Peak Density (10^{12}cm^{-3})
5
4
3
2
1
0
Total Particles (10^{15}cm^{-1})
3
2
1
0
0
10
20
30
40
Gas Fueling Rate (Torr-liters/sec)

Figure 4

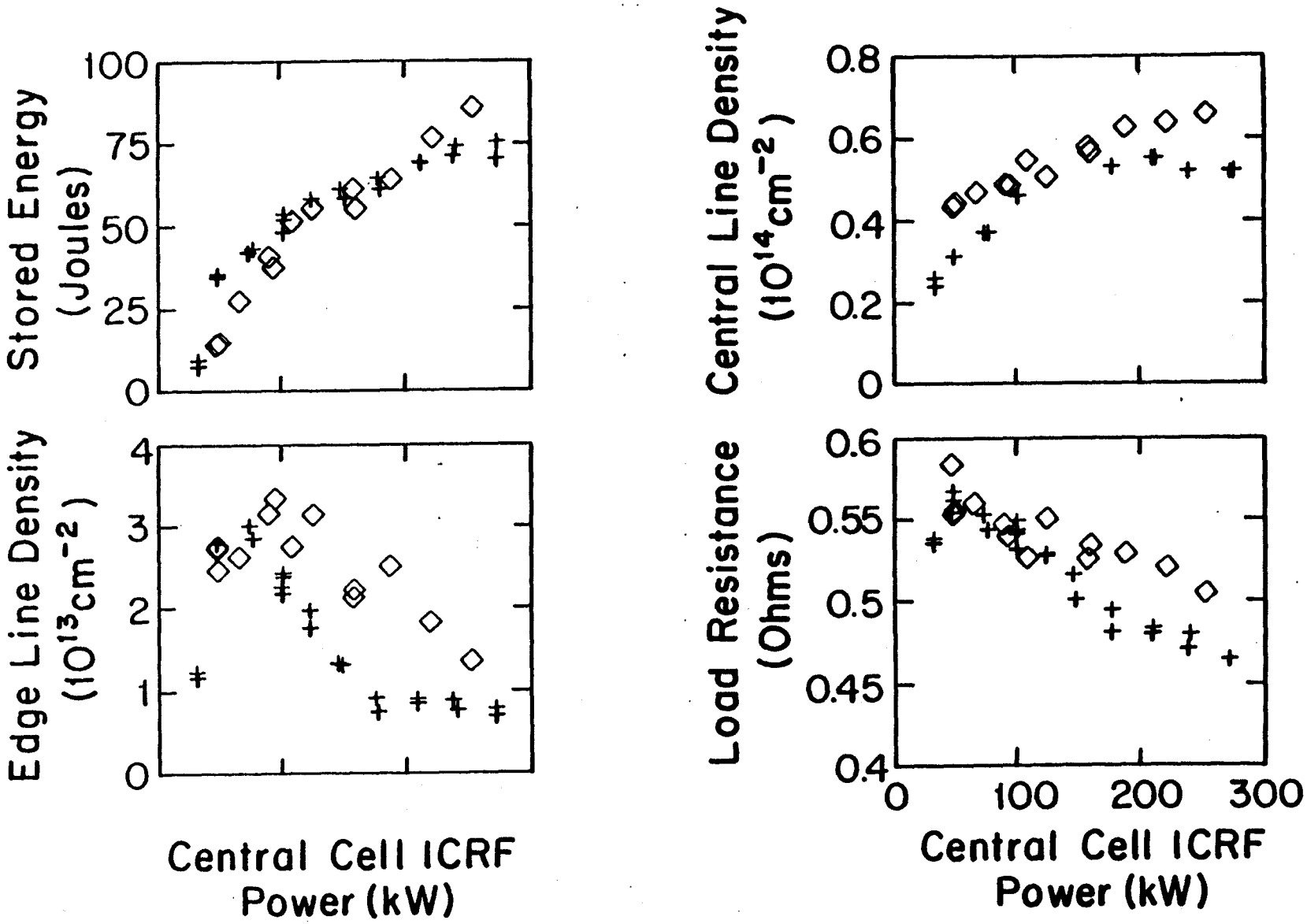
Stored Energy (Joules)
100
75
50
25
0
Edge Line Density (10^{13}cm^{-2})
4
3
2
1
0
Central Cell ICRF Power (kW)
Central Line Density (10^{14}cm^{-2})
0.8
0.6
0.4
0.2
0
Load Resistance (Ohms)
0.6
0.55
0.5
0.45
0.4
0
100
200
300
Central Cell ICRF Power (kW)

Figure 5

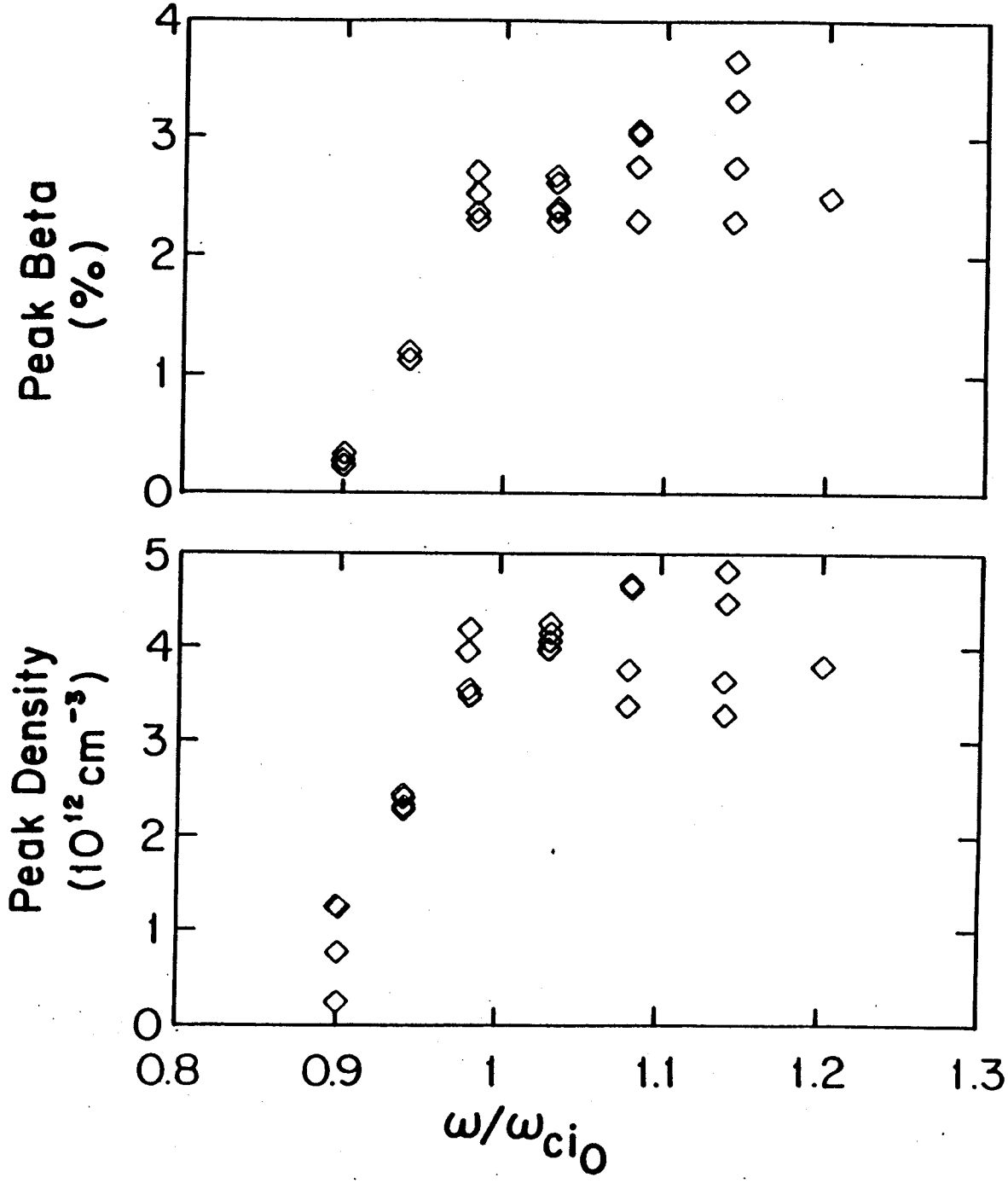
Peak Beta
(%)
4
3
2
1
0
Peak Density
(10^{12}cm^{-3})
5
4
3
2
1
0
0.8
0.9
1
1.1
1.2
1.3
ω/ω_{ci_0}

Figure 6

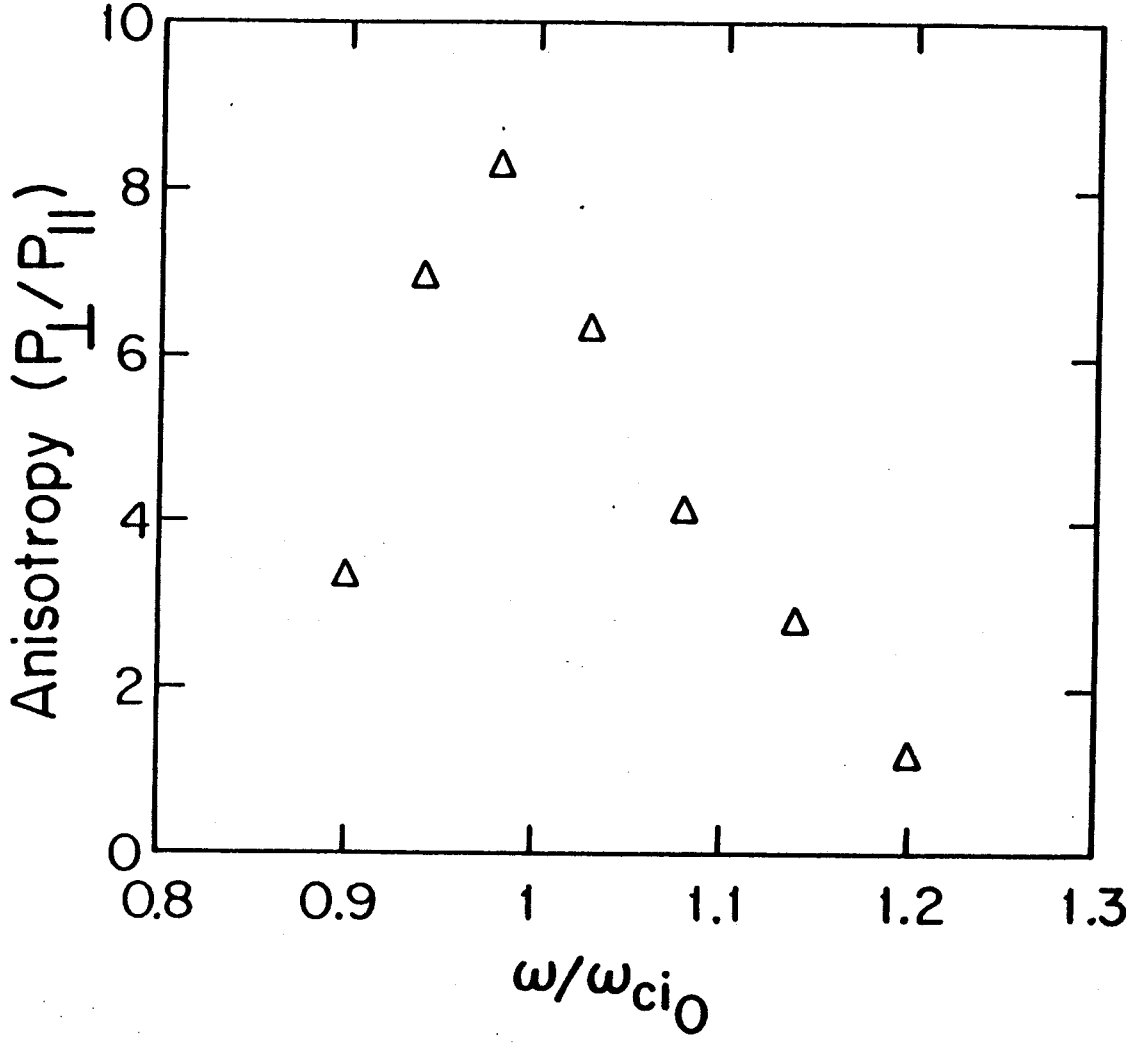

Figure 7

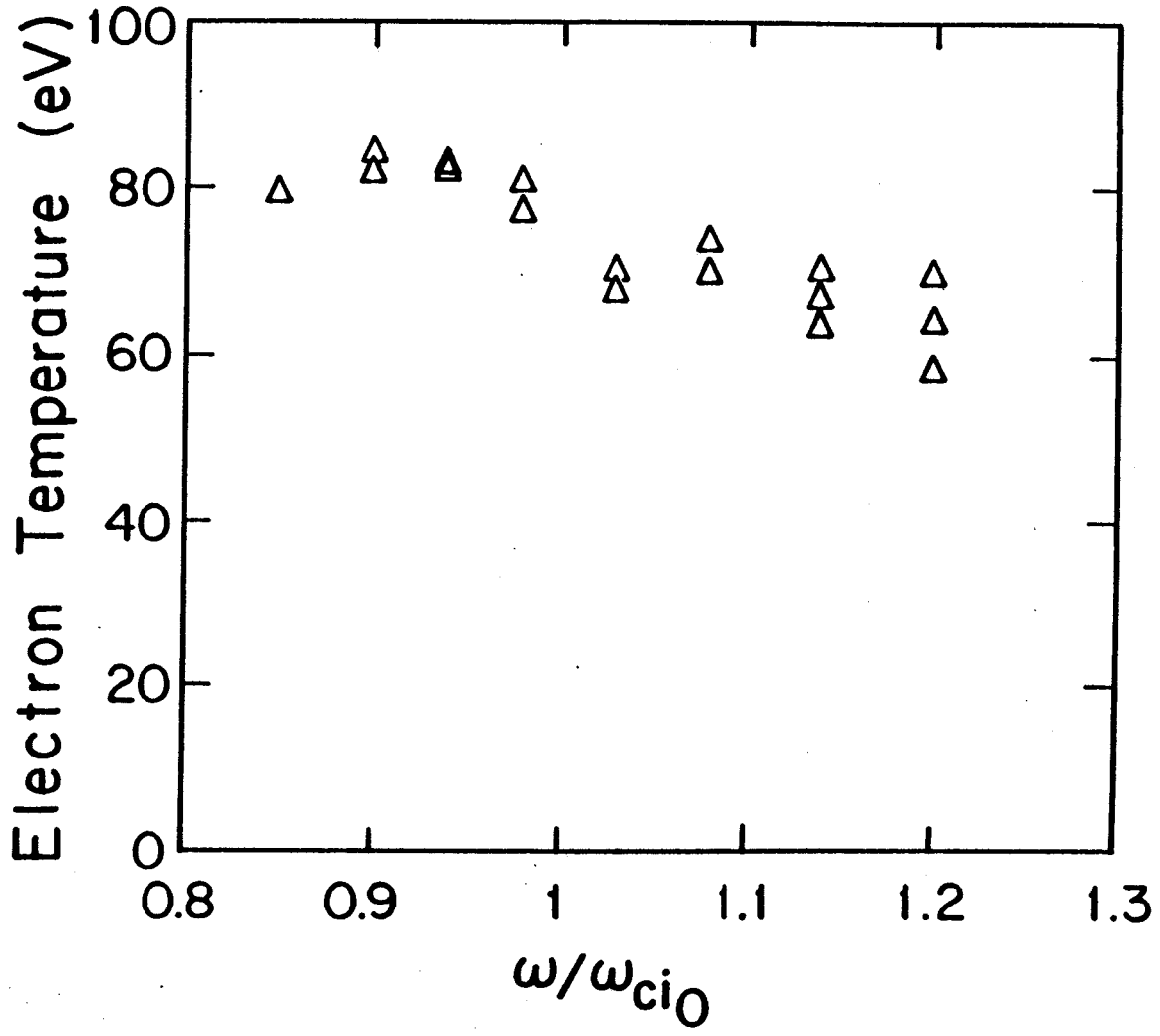
Electron Temperature (eV)
100
80
60
40
20
0
0.8
0.9
1
1.1
1.2
1.3
ω/ω_{ci_0}

Figure 8

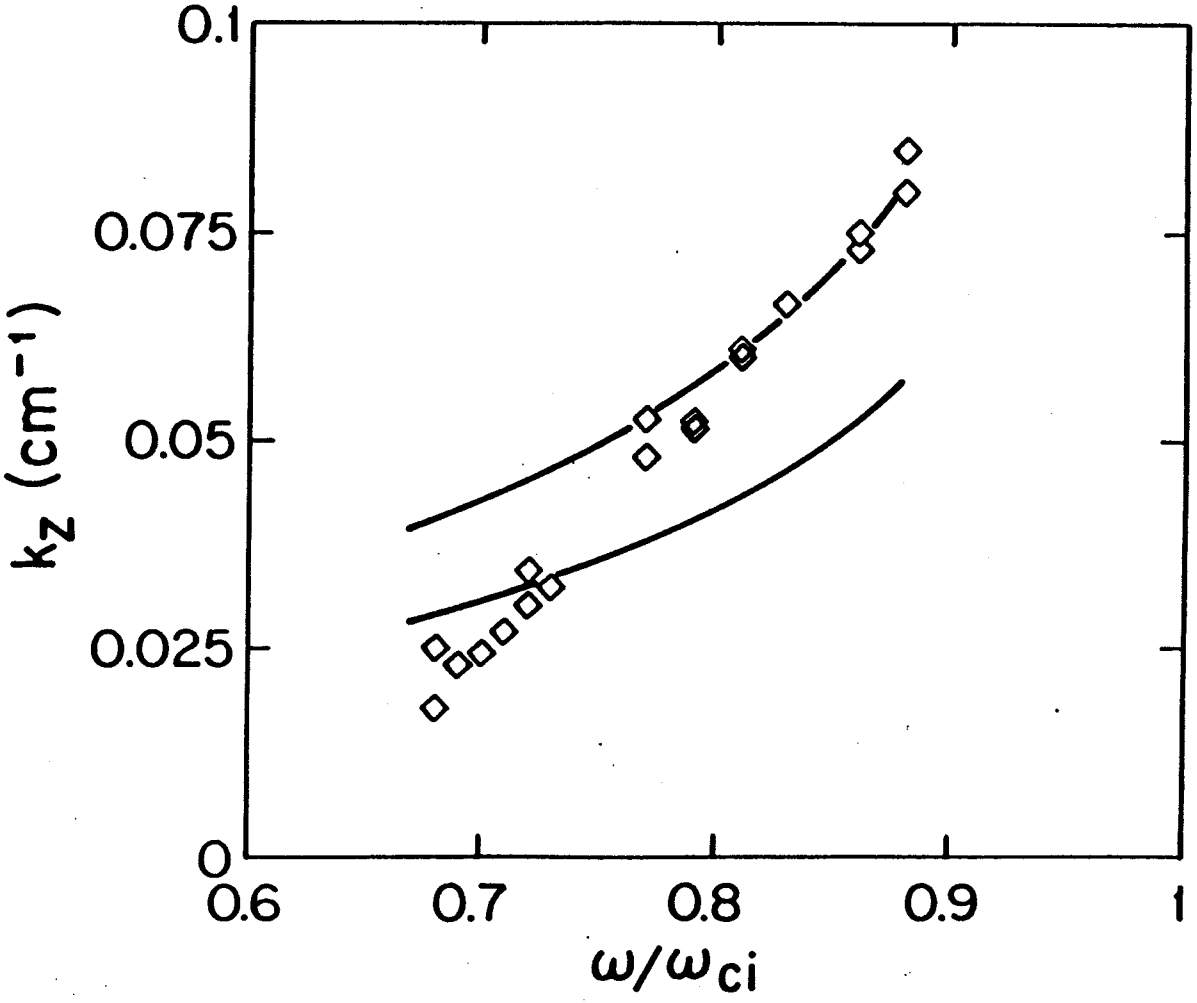

Figure 9

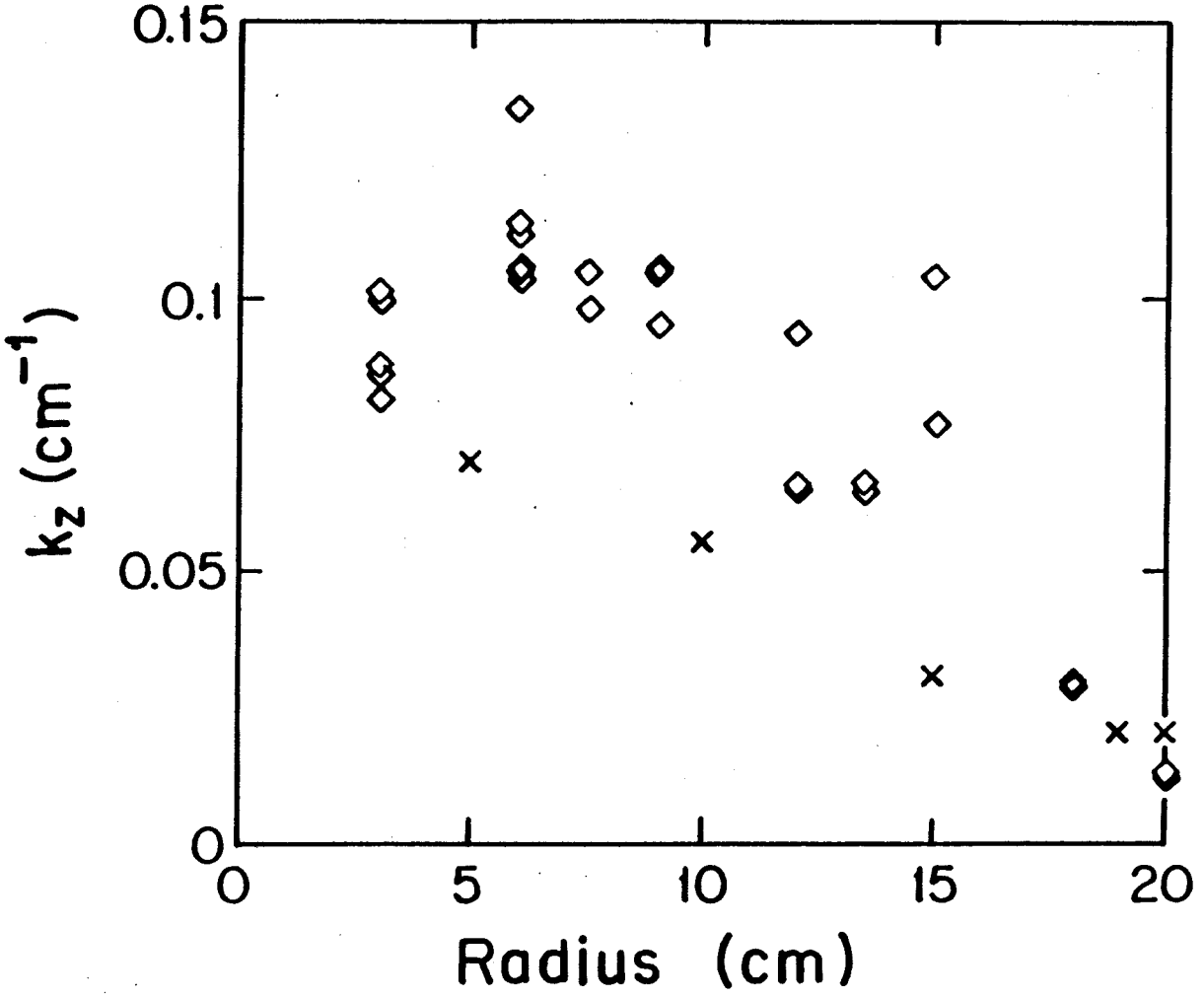

Figure 10

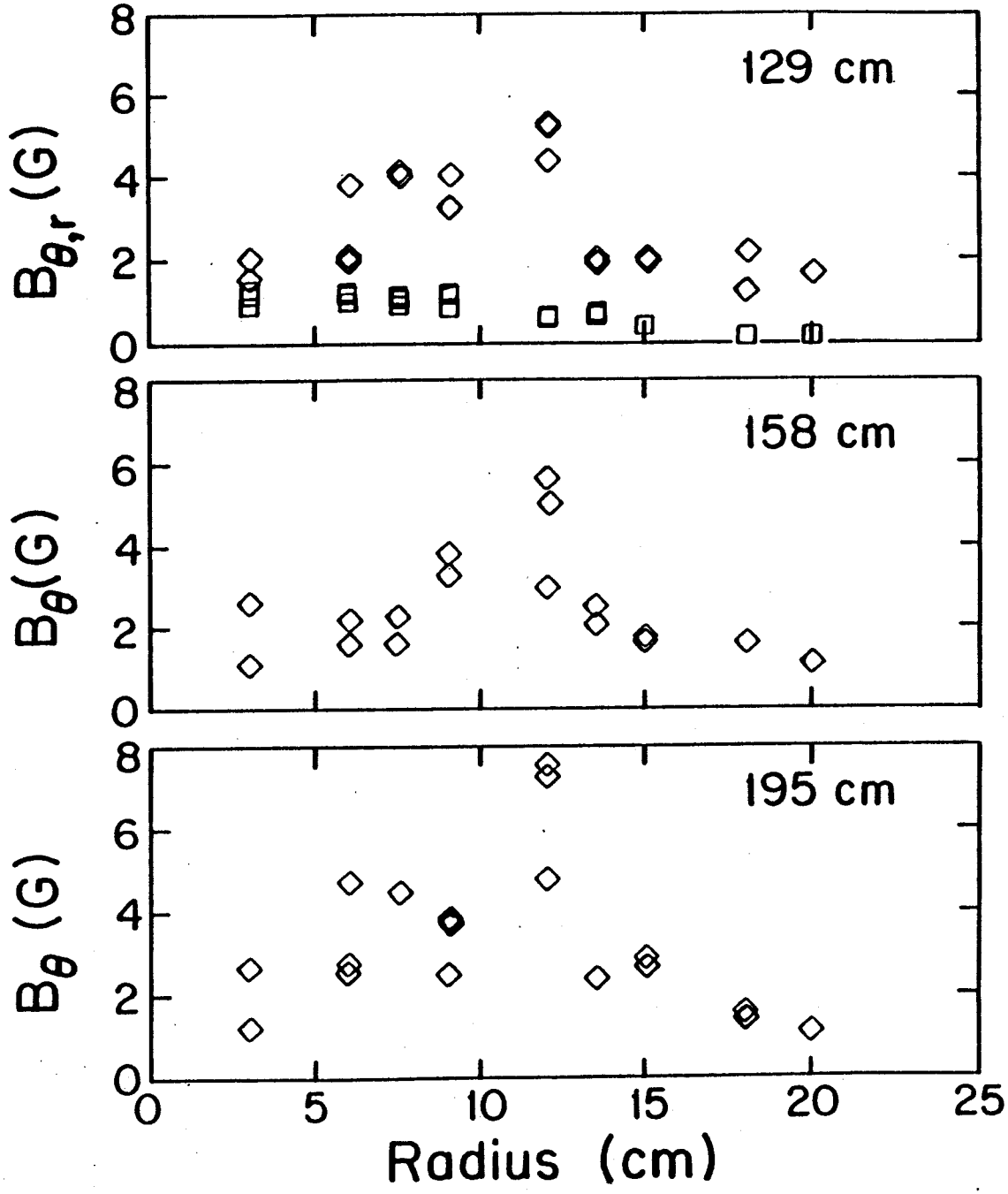
129 cm
158 cm
195 cm
$B_{\theta,r}$ (G)
B_θ(G)
B_θ (G)
Radius (cm)
0
2
4
6
8
0
5
10
15
20
25

Figure 11

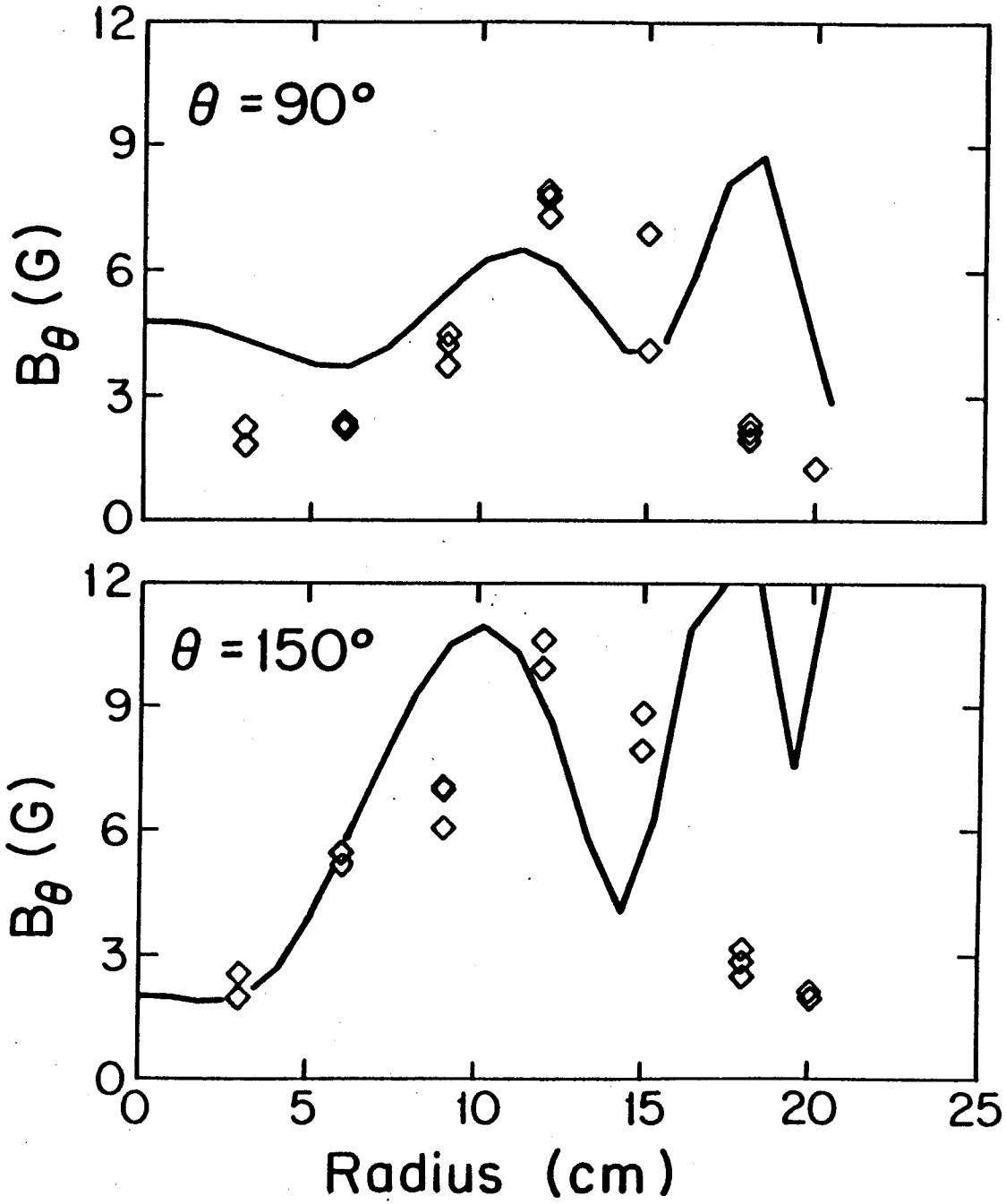

Figure 12